PAPER

Nickel(II) complexes based on dithiolate–polyamine binary ligand systems: crystal structures, hirshfeld surface analysis, theoretical study, and catalytic activity study on photocatalytic hydrogen generation†

Suman Adhikari, [ID] *[a] Tirtha Bhattacharjee,[b] Sharmila Bhattacharjee, [ID] [a] Constantin Gabriel Daniliuc, [ID] [c] Antonio Frontera, [ID] *[d] Eric M. Lopato[e] and Stefan Bernhard [ID] [e]

To ascertain the influence of binary ligand systems [1,1-dicyanoethylene-2,2-dithiolate (i-mnt $^{-2}$) and polyamine {tetraen = tris(2-aminoethyl)amine, tren = diethylene triamine and opda = o-phenylene-diamine}] on the coordination modes of the Ni(II) metal center and resulting supramolecular architectures, a series of nickel(II) thiolate complexes [Ni(tetraen)(i-mnt)](DMSO) (1), [Ni$_2$(tren)$_2$(i-mnt)$_2$] (2), and [Ni$_2$(i-mnt)$_2$(opda)$_2$]$_n$ (3) have been synthesized in high yield in one step in water and structurally characterized by single crystal X-ray crystallography and spectroscopic techniques. X-ray diffraction studies disclose the diverse i-mnt $^{-2}$ coordination to the Ni $^{+2}$ center in the presence of active polyamine ligands, forming a slightly distorted octahedral geometry (NiN$_4$S$_2$) in 1, square planar (NiS$_4$) and distorted octahedral geometries (NiN$_6$) in the bimetallic co-crystallized aggregate of cationic [Ni(tren)$_2$]$^{+2}$ and anionic [Ni(i-mnt)$_2$]$^{-2}$ in 2, and a one dimensional (1D) polymeric chain along the [100] axis in 3, having consecutive square planar (NiS$_4$) and octahedral (NiN$_6$) coordination kernels. The N–H⋯O, N–H⋯S, N–H⋯N, N–H⋯S, N–H⋯N, and N–H⋯O type hydrogen bonds stabilize the supramolecular assemblies in 1, 2, and 3 respectively imparting interesting graph-set-motifs. The molecular Hirshfeld surface analyses (HS) and 2D fingerprint plots were utilized for decoding all types of non-covalent contacts in the crystal networks. Atomic HS analysis of the Ni $^{+2}$ centers reveals significant Ni–N metal–ligand interactions compared to Ni–S inter-actions. We have also studied the unorthodox interactions observed in the solid state structures of 1–3 by QTAIM and NBO analyses. Moreover, all the complexes proved to be highly active water reduction co-cat-alysts (WRC) in a photo-catalytic hydrogen evolution process involving iridium photosensitizers, wherein 2 and 3 having a square planar arrangement around the nickel center(s) – were found to be the most active ones, achieving 1000 and 1119 turnover numbers (TON), respectively.

[a]Department of Chemistry, Govt. Degree College, Dharmanagar, Tripura (N)-799253, India. E-mail: sumanadhi@gmail.com
[b]Department of Chemistry, Bineswar Brahma Engineering College, Kokrajhar-783370, Assam, India
[c]Organisch-Chemisches Institut, Westfälische Wilhelms-Universität Münster, Corrensstraße 40, D-48149 Münster, Germany
[d]Department de Quimica, Universitat de les Illes Balears, Crta. de Valldemossa km 7.5, 07122 Palma de Mallorca, Baleares, Spain. E-mail: toni.frontera@uib.es
[e]Department of Chemistry, Carnegie Mellon University, 4400 Fifth Avenue, Pittsburgh, Pennsylvania 15213, USA
† Electronic supplementary information (ESI) available. CCDC 2054290–2054292. For ESI and crystallographic data in CIF or other electronic format see DOI: 10.1039/d1dt00352f

Introduction

On account of their application as potential building blocks in supramolecular materials with electrical conductivity, molecular magnetism, optoelectronic properties, and catalytic properties, metal complexes with sulphur rich ligands are currently of considerable interest.[1] Notably, binary ligand dithiolate based metal complexes have emerged as the most dynamic fields of chemistry due to their significance in the context of bioinorganic chemistry, versatile coordination chemistry, materials properties, and industrial applications.[2] Nickel–thiolate complexes have attracted a great deal of attention due to their highly delocalized extending systems and noteworthy building blocks for the preparation of certain

advanced materials with unusual catalytic and magnetic properties.[3] Given the facile redox states, potential for diverse ligations, and natural occurrence of Ni in [NiFe] hydrogenases,[4] studying the activity of these unique Ni species as water reduction cocatalysts (WRCs) was a logical step. In particular, the discovery of nickel–thiolate complexes for photocatalytic and electrocatalytic hydrogen production in EtOH/H$_2$O solvent mixtures[5] strongly invigorated the investigation of Ni–thiolate complexes in the construction of supramolecular architectures having potential applications in photo-catalytic hydrogen evolution.

Metal complexes incorporated with sulphur-based multifunctional ligands such as 1,1-dicyanoethylene-2,2-dithiolate (i-mnt^{-2}) and its geometric isomer 1,2-dicyanoethylene dithiolate (mnt^{-2}) are remarkable for their wide-range π-electron delocalizations and reversible redox behaviour and have been a subject of notable consideration.[6] The ligand i-mnt^{-2} represents an especially intriguing multifunctional building block owing to the presence of two anionic sulphur atoms and two nitrogen atoms of cyanide groups capable of binding to metal ions, for both complexation and non-covalent interactions and thus can be utilized to develop metal organic frameworks with unique properties.[7] The blend of coordination features and non-covalent interaction feasibilities ensure the rich metallo–supramolecular chemistry/coordination frameworks of i-mnt^{-2} based complexes. Regarding the above considerations, i-mnt^{-2} with bridging capacity and multiple binding sites is a good choice for the formation of supramolecular structures in combination with other N-donor polyamine ligands. Although extensive effort has been devoted to the problem of the design and synthesis of nickel–thiolate binary ligand complexes, the number of accessible frameworks, particularly with crystallographic evidence, remains limited and the physical property determinants remain recondite. The above aspects increased our enthusiasm for exploring the chemistry of nickel–thiolate complexes. The amalgamation of the electronic, structural, and binding properties of i-mnt^{-2} and appropriate N-donor polyamine ligands endows cooperative electronic materials with potential applications.

In this article, we report the use of simple binary ligand based complexes assembled from nickel salt with i-mnt^{-2} and polyamines in one step in water as highly active water reduction catalysts. We also employed our characterization techniques including classical structural description along with HS analysis and DFT calculations of interaction energies in order to quantify the energetic contributions of different non-covalent contacts to these structural features. Moreover, the structural descriptions of the synthesized complexes were also substantiated with HS analysis and DFT calculations. Since the numerous non-covalent interactions present in the supramolecular system offer the prospect towards a deeper understanding of the complicated processes regulating the supramolecular design, the selectivity/reactivity of chemical transformations is regulated by these weak non-covalent forces.[8] Catalytic experiments herein were performed using iridium photosensitizers. Cationic iridium(III) complexes have shown significant ability in photocatalytic reactions,[9] namely

water reduction,[10] due to their long-living, charge separated triplet excited state induced by spin–orbit coupling from the iridium center.[11] There are a variety of highly active mononuclear Ni WRCs including similar bonding moieties, namely, thiolate[12] and tetraaza-macrocycles.[13] Binuclear and polynuclear Ni complexes have also played a significant role in photocatalytic water reduction.[14]
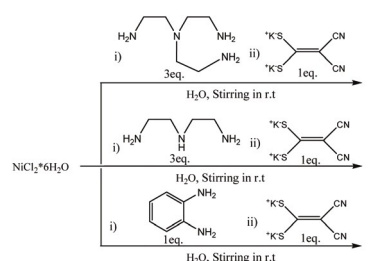
Experimental

Materials and physical measurements

All chemicals were of reagent grade and obtained from commercial sources and used without purification. The solvents were purified by standard procedures. 1,1-dicyano-2,2-ethylene-dithiolate dipotassium salt (K$_2$i-mnt) was synthesized according to the procedure reported previously.[15] Infrared spectra were measured on a Perkin-Elmer FT-IR spectrometer with KBr pellets in the range of 4000–500 cm^{-1}. NMR spectra were recorded on a Bruker Advance II (400 MHz) spectrometer using the residual protic solvent resonance as the internal standard and chemical shifts were expressed in ppm. Elemental analysis was carried out using a PerkinElmer 2500 series II elemental analyzer. Cyclic voltammetry was performed using a three-electrode system on a CH-Instruments Electrochemical Analyzer 600C potentiostat. All scans were performed at a rate of 0.1 V s^{-1} with negative scan polarity. UV-vis spectra were recorded on a Perkin Elmer model Lambda 25.

Synthesis of the metal complexes

The complexes were synthesized in one step in water with high yields. A schematic representation of the synthetic procedure is shown in Scheme 1.

A solution of NiCl$_2$·6H$_2$O (1.27 mmol) in 20 mL of distilled water was added slowly to ligand tetraen (3.81 mmol) dissolved in 20 mL water, with constant stirring at room temperature, and stirring was continued for 1 h. K$_2$i-mnt·H$_2$O (1.27 mmol) dissolved in 20 mL water was added with stirring to this reaction mixture, resulting in the immediate formation of a precipitate and stirring was continued for further 1 h. The precipitate obtained was filtered, washed several times with distilled water and ether, and dried in vacuo over fused CaCl$_2$. Single crystals of 1 were grown from the saturated solution of dimethyl sulphoxide (DMSO). IR, ^{1}H NMR and UV-Vis data are given in the

Scheme 1   Schematic representation of the synthetic procedure.

Experimental section and in the ESI.† For complex 1 and 2 the NMR spectra were dominated by the paramagnetic properties of the complexes and no significant peaks were detected.

Complex 1. Yield: 81%, FTIR (v cm^{-1}, KBr): 3297–3251 {v(N–H) asymmetric and symmetric stretching modes}, 2201 (vCN stretching), 1582 (vN–H bending scissoring vibration), 1366–1316 {v(CvC) absorption band}, 985 {v(vCS$_2$) group}, 887 {v(C–S)}. UV-vis. (4% DMSO in CHCl$_3$, λ$_{max}$/nm): 317, 356, 546. Anal. calc. for C$_{12}$H$_{24}$N$_6$NiOS$_3$: C, 34.05; H, 5.72; N, 19.86%. Found: C, 34.03; H, 5.69; N, 9.83%.

The synthetic procedures for 2 and 3 were similar to that of 1, except that ligands tren and opda were used instead of ligand tetraen. Single crystals of 2 and 3 were grown from the saturated solution of N,N-dimethyl formamide (DMF).

Complex 2. Yield: 84%, FTIR (v cm^{-1}, KBr): 3336–3260 {v(N–H) asymmetric and symmetric stretching modes}, 2203 (vCN stretching), 1584 (vN–H bending scissoring vibration), 1401–1380 {v(CvC) absorption band}, 964 {v(vCS$_2$) group}, 893 {v(C- S) band}. UV-vis. (4% DMSO in CHCl$_3$, λ$_{max}$/nm): 318, 414, 603. Anal. calc. for C$_{16}$H$_{26}$N$_{10}$Ni$_2$S$_4$: C, 31.81; H, 4.34; N, 23.19%. Found: C, 31.83; H, 4.33; N, 23.17%.

Complex 3. Yield: 82%, ^{1}H NMR (400 MHz, DMSO-d$_6$, δ in ppm): 6.40 (d, 4H, Ar–H), 4.30 (brs, 4H, –NH$_2$). FTIR (v cm^{-1}, KBr): 3552–3360 {v(N–H) asymmetric and symmetric stretching modes}, 2203 (vCN stretching), 1569 (vN–H bending scissoring vibration), 1368 {v(CvC) absorption band}, 948 {v(vCS$_2$) group, 899 {v(C–S) band}. UV-vis. (4% DMSO in CHCl$_3$, λ$_{max}$/nm): 317, 371, 434. Anal. calc. for C$_{26}$H$_{30}$N$_{10}$Ni$_2$O$_2$S$_4$: C, 41.08; H, 3.98; N, 18.42%. Found: C, 41.06; H, 3.99; N, 18.44%.

X-ray crystallography data collection and structure refinement

For compounds 1, 2, and 3 data sets were collected with a Nonius Kappa CCD diffractometer. Programs used: data collection, COLLECT;[16] data reduction Denzo-SMN;[17] absorption correction, Denzo;[18] structure solution SHELXT-2015;[19] structure refinement SHELXL-2015.[20] R-Values are given for the observed reflections, and wR^2 values are given for all reflections. In 1, the DMSO is disordered over two positions, and to the improve refinement stability, several restraints (SADI, SAME, ISOR and SIMU) were used. A summary of the crystallographic data and structure refinement details for 1–3 are given in Table 1. All bond lengths, bond angles and torsion angles of complexes 1–3 are depicted in Tables S1–S3.†

Hirshfeld surface analysis

The 3D Hirshfeld surfaces (HS) and 2D fingerprint plots[21–24] for 1–3 were obtained by using the Crystal Explorer 17.5 program package.[25] The 3D Hirshfeld surfaces were mapped over d$_{norm}$, shape index and curvedness,[22] where each point on the surface reveals information about d$_i$, d$_e$, and vdW; the surface point to the nearest interior nucleus distance, surface point to the nearest exterior nucleus distance and van der Waals radii of atoms respectively. The d$_{norm}$[23] parameter is defined as:

$$d_{norm} = \frac{d_i - r_i^{vdW}}{r_i^{vdW}} + \frac{d_e - r_e^{vdW}}{r_e^{vdW}} :$$

The red, white, and blue regions on the HSs represent shorter contacts (d$_{norm}$ −ve), contacts in the range of van der

Table 1 Crystal data and structure refinement summary for 1–3

	1	2	3
Empirical formula	C$_{12}$H$_{24}$N$_6$NiOS$_3$	C$_{16}$H$_{26}$N$_{10}$Ni$_2$S$_4$	C$_{26}$H$_{30}$N$_{10}$Ni$_2$O$_2$S$_4$
Formula weight	423.26	604.13	760.26
Temperature/K	173(2)	173(2)	173(2)
Crystal system	Monoclinic	Monoclinic	Monoclinic
Space group	P2$_1$/n	C2/c	C2/m
a/Å	8.3663(2)	16.3199(6)	18.658(4)
b/Å	14.6831(3)	9.1021(3)	7.2167(14)
c/Å	15.5009(4)	18.1332(7)	14.534(3)
α/°	90	90	90
β/°	99.3820(10)	114.143(3)	120.13(3)
γ/°	90	90	90
V/Å^3	1878.71(8)	2457.99(16)	1692.69(7)
Z	4	4	2
ρ$_{cal}$/g cm^{-3}	1.496	1.633	1.492
μ/mm^{-1}	1.377	1.898	1.400
F(000)	888	1248	784
Crystal size/mm^3	0.020 × 0.060 × 0.080	0.020 × 0.030 × 0.060	0.020 × 0.060 × 0.090
θ range/°	4.08–28.20	4.37–28.17	4.21–28.20
Reflections collected	8391	5608	3885
Independent reflections	4553 [R$_{int}$ = 0.0312]	2999 [R$_{int}$ = 0.0512]	2226 [R$_{int}$ = 0.0338]
Absorption correction	Multi-scan	Multi-scan	multi-scan
Max and min transmission	0.973 and 0.898	0.9630 and 0.8950	0.9730 and 0.8840
Data/restraints/parameters	4553/64/257	2999/0/167	2226/67/150
Goodness-of-fit on F^2	1.053	1.025	1.046
Final R indices [I > 2σ(I)]	R$_1$ = 0.0383, wR$_2$ = 0.0916	R$_1$ = 0.0495, wR$_2$ = 0.1053	R$_1$ = 0.0464, wR$_2$ = 0.1177
Final R indices [all data]	R$_1$ = 0.0463, wR$_2$ = 0.0963	R$_1$ = 0.0673, wR$_2$ = 0.1148	R$_1$ = 0.0564, wR$_2$ = 0.1261
Largest difference in peak and hole/e Å^3	0.403 and −0.729	0.438 and −0.43	0.626 and −0.439

Waals separation (d_{norm} = 0) and longer contacts (d_{norm} + ve), respectively.

Theoretical methods

The calculations reported herein were carried out using Gaussian-09[26] at the B3LYP/def2-TZVP level of theory. Bader's quantum theory of "Atoms in molecules" QTAIM has been used to study the interactions discussed herein by means of the AIMall calculation package.[27] The calculations of the wave-function and NBO 3.0 (Natural Bonding Orbital) calculations were carried out at the same level of theory.

Photocatalytic hydrogen evolution

Analyses of compounds 1, 2, and 3 as water reduction cocatalysts (WRCs) for photocatalytic reactions were performed in a unique parallelized photoreactor.[28] The well-studied [Ir (Fmppy)$_2$dtbbpy]PF$_6$ (where Fmppy = 4′-fluoro-2-phenyl-5-methylpyridine, dtbbpy = 4,4′-di-tert-butyl-2,2′-bipyridine)[29] compound was utilized as a photosensitizer (PS) in this system. 1 mL of shell vials were populated with 600 microliters of PS and WRC solutions in DMSO (J.T. Baker JT 9224), and 150 microliters of a 30% (w/w) solution of triethanolamine (TEOA) (Alfa Aesar L04486) in water, as a sacrificial electron donor. The reactions involved a range of PS concentrations from 0 to 0.75 mM and WRC concentrations ranging from 0 to 0.1 mM, and were illuminated using water cooled 100 W blue light-emitting diodes (LEDs) (440 ± 10 nm) for 1000 minutes, and monitored every 10 minutes by photography with a commercially available colorimetric hydrogen sensitive tape (DetecTape Hydrogen Detection Tape – Midsun Specialty Products, Item DT-H210015-PF4). These images were processed through a Wolfram Mathematica Script to determine the quantity of hydrogen produced with time.

Results

Recapitulation of the crystal structures

[Ni(tetraen)(i-mnt)](DMSO). Single crystal XRD analysis revealed that the complex [Ni(tetraen)(i-mnt)](DMSO) (1) crystallises in the monoclinic crystal system with the space group P2$_1$/n, and the asymmetric unit is composed of one Ni(II) ion, tetraen, i-mnt^{-2}, and one solvent molecule (DMSO) disordered over two positions as shown in Fig. 1. In 1, Ni^{+2} is hexa-coordinated with the NiN$_4$S$_2$ coordination environment and exhibits a distorted octahedral geometry where the Ni(II) metal center is coordinated to four amino N-atoms (N3, N4, N5, N6) of archetypal tripodal flexible chelate tetraen in a trichelated fashion and i-mnt^{-2} is chelated to Ni^{+2} through two thiolate S-atoms (S1, S2) providing overall neutrality for the coordination sphere while the two cyano ends of i-mnt^{-2} remain free. In the slightly distorted octahedral geometry of 1, S1, S2, N4, and N5 occupy the corners of the basal plane and the axial sites are occupied by N3 and N6 atoms where Ni^{+2} resides at the centre of the basal plane and the axial Ni–N bonds slightly tilt towards the tetraen moiety. The distortion around the Ni(II)
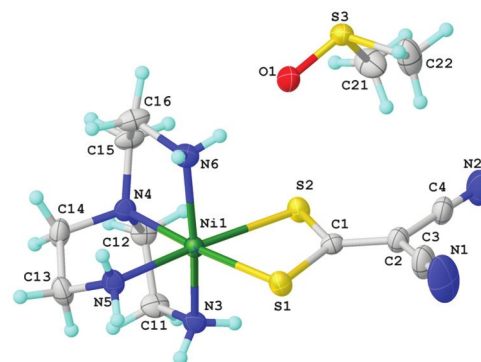

Fig. 1 Molecular structure of 1, showing the atom labelling scheme with 50% probability ellipsoids.

center is evident from the trans angles 162.9(1)^0 [N3–Ni1–N6] and 174.0(1)^0 [N5–Ni1–S2] which might be due to the intra and intermolecular interactions of the thiolate ends (i-mnt^{-2}) and the inherent tendency of tetradentate tetraen to offer a trigonal bipyramidal coordination cap to any metal center cannot be ruled out.[30–33] A similar attempt was made with Zn(II) salt, tetraen, and i-mnt^{-2} that showed a trigonal bipyramidal geometry[34] instead of octahedral. The solvent molecule, DMSO, offers stability to the crystal structure by forming intermolecular hydrogen bonds with the amino N–H donors. A summary of all the intermolecular interactions is depicted in Table S4.† The close proximity of the cyano end (i-mnt^{-2}) and sulfoxide S-atom of DMSO opens up the possibility of σ-hole chalcogen bonding interaction. The N–H···O and N–H···S type H-bonds and van der Waals interactions are believed to be responsible for the crystal stability. These H-bond connectors link the molecules forming a 3D supra-molecular stacking assembly along the ab plane (Fig. S10†). We can visualize a segment of the stacked assembly as a 3D right handed helical arrangement along the ac plane imagining the axis of the helix passing through the Ni(II) atoms of each asymmetric unit (Fig. 2). These repeating hydrogen bonds throughout the crystal structure generate finite chain, infinite chain, and ring geometrical arrays of graph-set-motifs D, C(6), C(4), R$_3^2$(8), R$_2^1$(6), and R$_4^2$(10), respectively.

[Ni$_2$(tren)$_2$(i-mnt)$_2$]. The complex [Ni$_2$(tren)$_2$(i-mnt)$_2$] (2) crystallises in the monoclinic crystal system, space group C2/c, with two halves of Ni^{+2} ions, one tren, and one i-mnt^{-2} in the asymmetric unit. The bimetallic chelate 2 exists as a co-crystallized aggregate of cationic [Ni(tren)$_2$]$^{+2}$ and anionic [Ni(i-mnt)$_2$]$^{-2}$ (Fig. 3). The two Ni^{+2} ions show hexa-coordinated and
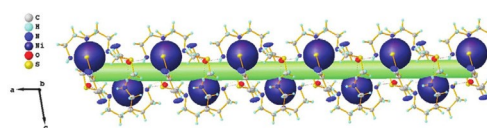

Fig. 2 Crystal packing arrangement as a 3D right handed helix along the ac plane.

tetra-coordinated environments and exhibit octahedral and square planar geometries, respectively. In NiS$_4$, four thiolate S-atoms (S1, S2, S1^{ii}, S2^{ii}) [(ii) −x + 1, −y + 1, −z] coordinated to Ni^{+2} in a trans bischelated fashion and occupy four corners of the square planar geometry. The Okuniewski parameter[35] τ'_4 = 0 [τ'_4 ¼ $\frac{\beta}{360°}$ $\frac{\alpha}{\theta}$ þ $\frac{180°}{180°}$ $\frac{\beta}{\theta}$, β > α and θ = cos^{-1}(−1/3) ~ 109.5°, where τ'_4 = 0 means a square planar, and τ'_4 = 1 means a tetrahedral geometry] confirms the square planar coordination kernel (β = 180.0° [S2–Ni1–S2^{ii}], α = 180.0° [S1–Ni1–S1^{ii}]).

In the NiN$_6$ coordination environment, six amino N-atoms (N3, N4, N5, N3^i, N4^i, N5^i) [(i) −x + 1, y, −z +$\frac{1}{2}$] of tren chelated to Ni^{+2} in a slightly distorted octahedral fashion where N3, N3^i, N4, and N4^i occupy the corners of the basal plane, and terminal amino N-atoms (N5 and N5^i) occupy the trans axial sites and the deviation of the Ni(II) metal center from the centroid of basal plane is 0.055(3) Å. The trans angles 171.5(1)° [N3–Ni2–N4^i] and 168.5(2)° [N5–Ni2–N5^i] and the bite angles varying in the range from 82.7(1)° to 102.8(2)° justify the distortion in the octahedral geometry. The normal angle, twist angle, and fold angle between the square planar plane (S1, S2, S1^{ii}, S2^i) and octahedral basal plane (N3, N3^i, N4, N4^i) are found to be 58.6(1)°, 55.4(1)°, and 49.5(1)° respectively. The Ni⋯Ni distances 5.592(1) Å [Ni1⋯N2], 9.102(1) Å [Ni1⋯Ni1] and 16.320(1) Å [Ni2⋯Ni2] [greater than the sum of the van der Waals radii of two Ni(II) atoms] confirm the absence of Ni(II)⋯Ni(II) metallophilic interaction.[36] A summary of all the hydrogen bond parameters is listed in Table S4.† The N4–H4⋯S1 intramolecular hydrogen bond is the only connector between the NiS$_4$ and NiN$_6$ coordination spheres and it forms a finite chain geometry of the D type graph-set-motif and the N–H⋯N type intermolecular H-bonds form an infinite chain geometry of the C(8) type graph-set-motif. Undoubtedly, the N–H⋯S and N–H⋯N H-bonds (Fig. S11†) along with van der Waals interactions contribute immensely to the stabilization of the crystal structure. These connectors interconnect the
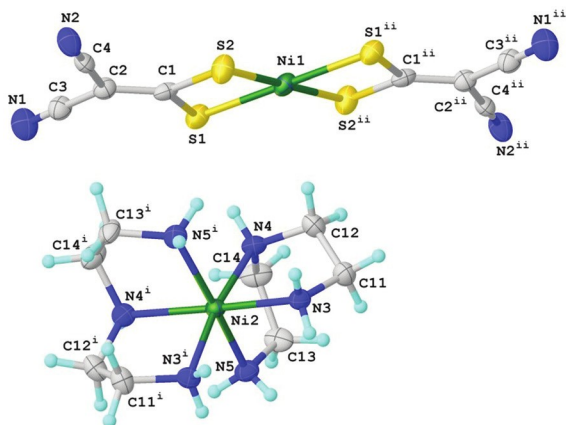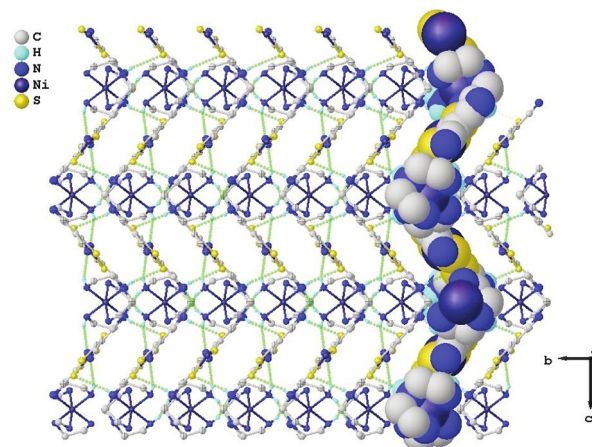

Fig. 4 Projection of 3D supramolecular stacked chains along the bc plane for 2 (hydrogen bonds as dotted lines).

molecules in 2 leading to the formation of 3D supramolecular zic-zac stacked chains along the bc plane as shown in Fig. 4.

[Ni$_2$(i-mnt)$_2$(opda)$_2$]$_n$. The complex [Ni$_2$(i-mnt)$_2$(opda)$_2$]$_n$ (3) crystallizes in the monoclinic crystal system, space group C2/m, and the asymmetric unit consists of two halves of Ni(II) ions, a complete i-mnt^{-2} ligand, half the opda molecule, and one solvent molecule (DMF) disordered over two positions. It is a binuclear Ni(II) polymeric complex having two discrete NiS$_4$ and NiN$_6$ coordination spheres linked via i-mnt^{-2} (Fig. 5). The S$_4$ donor set comprises four thiolate S-atoms (S1, S2, S1^i, S2^i) [(i) −x + 2, −y − 2, −z + 1] of two i-mnt^{-2} chelated to Ni^{+2} in a bischelated fashion generating a square planar geometry. The existence of a perfect square planar kernel is confirmed from the Okuniewski parameter[35] τ'_4 = 0 (β = 180.0 [S2–Ni1–S2^i], α = 180.0° [S1–Ni1–S1^i]). In NiN$_6$, Ni^{+2} is coordinated by two amino N-atoms (N3, N3^{ii}, N3^{iii}, and N3^{iv}) [(ii) −x + 2, −y − 2, −z; (iii) x, −y − 2, z; (iv) −x + 2, y, −z] of two opda in a bischelated fashion and two cyano N-atoms (N1, N1^{iii}) of two i-mnt^{-2}. The i-mnt^{-2} molecule in the presence of opda connects two nearby Ni^{+2} ions in a tridentate fashion through thiolate and cyano terminals, thereby forming a one dimensional (1D) infinite polymeric chain of consecutive NiS$_4$ and NiN$_6$ kernels which propagates along the [100] axis (Fig. 6). In
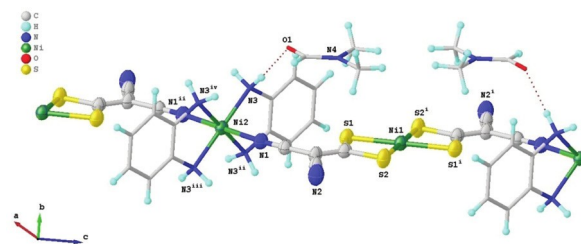

Fig. 3 Molecular structure of [Ni$_2$(tren)$_2$(i-mnt)$_2$] showing the atom labelling scheme with 50% probability ellipsoids (symmetry codes: (i) −x + 1, y, −z + $\frac{1}{2}$; (ii) −x + 1, −y + 1, −z).

Fig. 5 Perspective view of the polymeric segment showing the coordination environment around the Ni(II) metal center [symmetry code (i) −x + 2, −y − 2, −z + 1; (ii) −x + 2, −y − 2, −z; (iii) x, −y − 2, z; (iv) −x + 2, y, −z; (v) x + $\frac{1}{2}$, y + $\frac{1}{2}$, z].
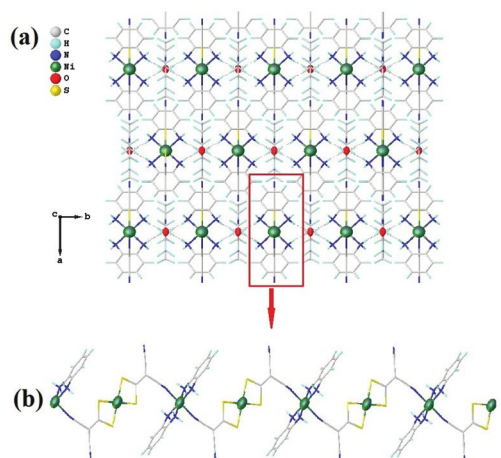
Fig. 6   (a) View of the 3D supramolecular assembly.   (b) Segment of the polymeric chain.

Fig. 7   View of   the 2D supramolecular   chain assembly along the bc plane. The N3–H3A⋯O1 hydrogen bonds shown as red dotted lines.

the octahedral   geometry of NiN$_6$, N3, N3^{ii}, N3^{iii}, and N3^{iv} (opda) occupy the corners of   the basal plane; N1, and N1^{iii} (i-mnt^{-2}) occupy the trans axial sites perpendicular to the basal plane and the metal center resides at the centroid of the basal plane. A small distortion in the octahedral   geometry is observed due to little variation in the bite angles ranging from 83.2(1)° to 96.8(1)°. All the Ni2–N [2.088(2) Å] bond lengths in the basal plane are found to be similar and the same trend is observed for the apical   Ni2–N bonds [2.110(3) Å]. The twist angle 90.0(2)° justifying the perpendicular arrangement of the square planar and octahedral basal plane contrary to 2 and the large Ni1⋯N2 [7.267(2) Å] distance discard the possibility of metallophilic   interaction.[36] The square planar geometry of NiS$_4$ in 2 and 3 is almost identical, in contrast, the octahedral kernels are quite different due to the influence of the secondary ligand (opda).   The distance between the   S1 atom of i-mnt^{-2} and the centroid of the phenyl ring (opda) [3.809(3) Å] exceeds the sum of van der Waals radii   (3.5 Å),[37] suggesting the absence of any anion⋯π interaction.

A summary of all hydrogen bond parameters is listed in Table S4.† The neutral DMF solvent molecules link the parallel 1D polymeric   chains via N3–H3A⋯O1 hydrogen bonds forming a 2D supramolecular chain like arrangement   along the ab plane assuming that the DMF molecules reside at the crystal voids and NiS$_4$ kernels (sp) perpendicular to the chain (Fig. 7). These N–H⋯O connectors among the two DMF and two NiN$_6$ moieties in the parallel polymeric chain,   generate a twelve membered ring like geometrical   array of   the R$_4^2$(12) graph-set-motif. These 2D packed chains are further   inter-connected via   N3–H3B⋯N2 hydrogen bonds   between the opda N3–H3B donors and free cyano end acceptors (N2)   of i-mnt^{-2}, which extends in a three dimension leading to the for-mation of   a 3D supramolecular circular ribbon like stacked assembly as shown in Fig.   S12.† The formation of   a twenty-eight membered ring like structure due to the N3–H3B⋯N2 connector can be assigned to the C(14)R$_2^2$(28) type graph-set-motif.
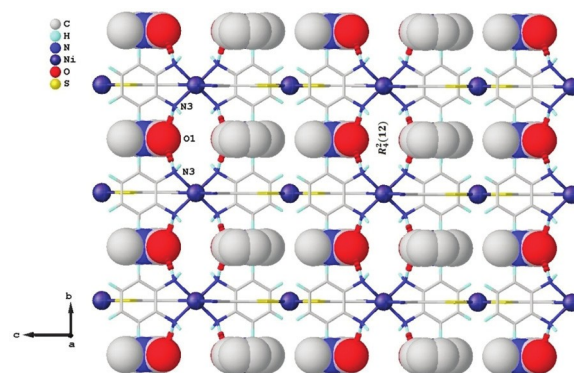
Hirshfeld   surface analysis. The Hirshfeld   surface (HS) analysis[21,22] and associated two dimensional (2D) fingerprint (FP) plots are exceedingly useful techniques that offer an unambiguous analysis of multicomponent crystal structures,[38] revealing a detailed immediate environment of a molecule and quantifying all possible non-covalent intermolecular inter-actions formed by the molecule in question thereby permitting a systematic comparison of related crystal structures.[39–41] The X-ray diffraction study reveals the fascinating coexistence of independent cationic (oc) and anionic (sp) species as cocrystal-line aggregates in 2 and a 1D polymeric chain in 3. These ver-satilities of binary ligand-based nickel complexes tempt us to explore further non-covalent interactions by the HS study. The HS mapped separately for the anionic [Ni(i-mnt)$_2$]$^{-2}$ [2A] and cationic [Ni(tren)$_2$]$^{+2}$ [2B] species in 2, while for 3, the square planar [3A] and octahedral [3B] segments in the repeating poly-meric unit [Ni$_2$(i-mnt)$_2$(opda)$_2$] are studied separately. The 3D HS mapped with d$_{norm}$ and the 2D FP plots   for 1–3 are depicted in Fig. 8 and 9. The standard (high) surface resolu-tion criterion was chosen and the surface transparency option allowed for a clear   visualization and identification of   inter-actions through the mapped surfaces. The requisite quantitat-ive information regarding the molecular volume (V$_H$), surface area (A$_H$), globularity (G), and asphericity (Ω) is given in Table 2. The octahedral 1, 2B, and 3B have higher Hirshfeld
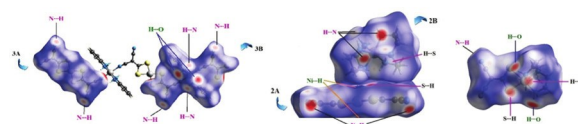

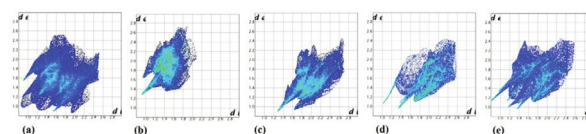Fig. 8   View of the Hirshfeld surfaces mapped over d$_{norm}$.

Fig. 9   2D fingerprint plots for (a) 1, (b) 2B, (c) 2A, (d) 3A, and (e) 3B.

Table 2 Quantitative data from the Hirshfeld surface of 1–3

Complex	V_H (Å^3)	A_H (Å^2)	G	Ω
1	360.72	304.19	0.806	0.120
2A	299.58	293.38	0.738	0.333
2B	302.18	259.32	0.840	0.033
3A	295.56	283.60	0.757	0.353
3B	569.44	486.80	0.682	0.150

volumes (V_H) and surface areas (A_H) expect 2B due to the compact shape. All the asymmetric units have a well defined 3D structured molecular surface as the globularity[42] values are less than one and 2B has the most convex HS. The asphericity[43] data clearly show the greater anisotropy properties of 2A and 3A (Table 2).

The intense red spots on the d_{norm} HS around the cyano end of i-mnt^{-2} (1, 2A, 3A), amino end of tetraen (2B) and opda (3B) indicate strong N⋯H/H⋯N intermolecular interactions arising from the N–H⋯N and C–H⋯N type hydrogen bonds (Table S4†) and the dull red spots observed around the thiolate end of i-mnt^{-2} (1, 2A) denote moderate S⋯H contacts due to the N–H⋯S hydrogen bonds. In contrast weak S⋯H contacts appear as white spots in 3A. The deep red spots in 1 and 3B observed for the strong H⋯O contacts are assigned to the $N_{coordinated\ tetraen}$–H⋯O_{DMSO} and $N_{coordinated\ opda}$–H⋯O_{DMF} hydrogen bonds, respectively.The remaining faded red regions and white areas on the HS originate from the weak C⋯H/H⋯C and H⋯H contacts respectively while the blue areas indicate the absence of any interaction. The HSs mapped on the shape index and curvedness are devoid of any red or blue triangles (bow-tie pattern) (Fig. S13†) and the observation of no flat surface patches nullifies the possibility of π⋯π and C–H⋯π interactions.

The two dimensional (2D) fingerprint plots for 1–3 based on d_i versus d_e in the translated range appeared as distinct upper donor and lower acceptor spikes, representing the N⋯H/H⋯N contacts around 2.2 Å < d_e + d_i < 2.8 Å (1, 2B, 3B), S⋯H/H⋯S contacts around 2.4 Å < d_e + d_i < 3.2 Å (Fig. 9 and Fig. S14, S15†) and C⋯H/H⋯C contacts around d_e + d_i ~ 2.8 Å. The sharp blue spikes, appeared around d_e + d_i ~ 2 Å, denote strong H⋯O contacts (1, 3B). The H⋯H contacts that bestow the crystalline lattice strength appeared as scattered points, spreading up to d_i = d_e = 2.5 Å for 1, 2.1 Å < d_i = d_e < 2.6 Å for 2B, and d_i = d_e = 2.4 Å for 3B. From the 2D FP plots it is obvious that apart from H⋯H and other minor contacts, the hydrogen bond interactions account for more than 50% of all contacts (1, 61.7%; 2A, 86%; 2B, 72%; 3A, 86.1%; 3B, 65.5%) which play a leading role in the supramolecular crystal packing. In 2A, the predominant S⋯H, and N⋯H contacts (34.0% and 35.4%) arise from the strong N–H⋯N and N–H⋯S hydrogen bonds (Table S4†) between 2B and 2A. The small but substantial Ni⋯H contact (3.5%) explains the possibility of C–H⋯Ni interaction (2.966 Å) between the anionic (2A) and cationic (2B) fragments (Fig. S16†).The H⋯N, H⋯S, and H⋯C contacts are found to be less in the octahedral complexes (1, 2B, 3B) compared to those in the square planar ones (2A, 3A). 3A, due to the 1D polymer formation via the cyano end of

i-mnt^{-2}, experiences lower N⋯H interaction (32.4%) compared to non-polymeric 2A, in fact, the latter has maximum N⋯H and S⋯H interactions compared to the former. The comparative distribution of the non-covalent interactions (percentage scale) is shown as a 3D stacked bar diagram in Fig. 10.

To evaluate the impact of the diverse ligand coordination to the metal center in 1–3, we have also performed HS analysis[44,45] on the nickel center. In contrast to the molecular HS, a slight change in the coordination direction or nature of the ligand impacts the HS of the metal center with significant depressions which in turn changes the HS properties like volume, globularity etc.[21–24] It is evident from the comparatively high volume, surface area, and globularity of the octahedral complexes (1, 2B, and 3B) compared to those of the square planar ones (2A and 3A) inferring further deviation of the surface area from that of a sphere for the latter (Table 3). Moreover, a huge difference in the asphericity (Ω) indicates much higher anisotropy in the square planar complexes compared to that in the octahedral ones evincing the fact that the metal complexes (2A and 3A), having longer coordination bonds, show a higher anisotropic metal surface. The larger volumes and surface areas of the square planar complexes also had an impact on the 2D FP plots revealing higher d_i and d_e limiting values. The Ni–N coordination bonds appeared as circular bright-red spots perpendicular to the Ni–N bond direction on the HS mapped over d_{norm} (Fig. 11). The Ni–N bond
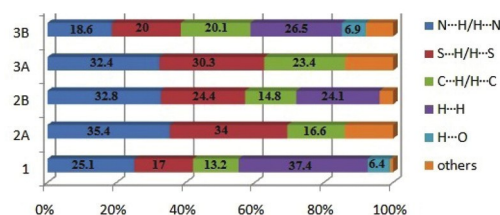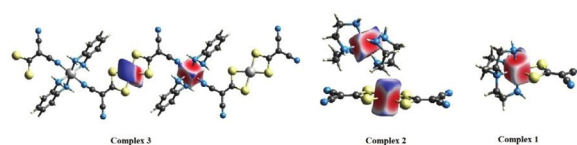

Fig. 10 Stacked bar diagram illustrating the relative distribution of interactions from HS analysis for 1–3.

Table 3 Quantitative data from the Hirshfeld surface of the Ni–metal centers in 1–3

Ni^{+2} in	V_H (Å^3)	A_H (Å^2)	G	Ω
1	11.09	28.12	0.855	0.025
2A	13.50	31.71	0.864	0.099
2B	10.82	28.00	0.854	0.016
3A	16.71	37.47	0.844	0.188
3B	10.63	28.42	0.823	0.019

Fig. 11 View of the Hirshfeld surfaces for the nickel center in 1–3 mapped over d_{norm}.

strength is evident from the rectangular orange spots and green flat regions on the HS mapped with the shape-index (S) and over curvature (C), respectively (Fig. S13†). The slight differences in the Ni–S bond lengths are evident from the irregular orange patches surrounded by yellow regions on the HS mapped over the shape-index (Fig. S13†). The sulphur atoms coordinated to the Ni-centers through the regions outside the orange patches on the HS indicate the deviations of the Ni–S bonds from the normal of the surfaces. In the 2D FP plots, the prominent long red spikes at $d_e + d_i \approx 2.1$ Å indicate the Ni–N bonds for 1 (lower spike), 2B and 3B; whereas the red spikes at $d_e + d_i < 2.4$ Å indicate the Ni–S bonds for 1 (upper spike), 2A and 3A (Fig. 12). The 2D FP shows the contributions of the Ni–N and Ni–S co-ordinations which are in the order of 3B (78.3%) > 2B (73.7%) > 1 (53.6%) and 3A (59.8%) > 2A (56.3%) > 1 (24.7%), respectively. Furthermore, the Ni⋯H contacts in square planar complexes 3A (40.2%) and 2A (43.8%) have a higher contribution, compared to those in octahedral complexes 1 (21.6%), 2B (26.3%), and 3B (21.7%).

Theoretical study of the complexes

Experimentally, three new Ni(II) complexes have been synthesized and X-ray characterized. The theoretical analysis is devoted to the study of some unorthodox interactions observed in the solid state of these compounds using two different computational techniques: (i) the QTAIM analysis to confirm the existence and characterize the interactions and (ii) the NBO analysis to investigate if the orbital donor–acceptor interactions are energetically relevant.

In compound 1, we have analyzed one of the interaction modes of the complex with the co-crystalized DMSO solvent molecule. In Fig. 13a we show a partial view of the solid state structure of 1 and DMSO where it can be observed that the N

atom of the i-mnt^{-2} co-ligand points to the S-atom of DMSO opposite to the S–CH$_3$ bond. This is typical of σ-hole chalcogen bonding interactions. We have performed the QTAIM analysis to confirm the existence of this interaction by examining the distribution of bond critical points (CPs) and bond paths of the dimer, as shown in Fig. 13b. The chalcogen bond is characterized by the existence of a bond CP (the green sphere) and bond path interconnecting the N and S atoms, thus confirming the interaction. Moreover, an additional bond CP and bond path connect the N atom to one H-atom of the methyl group, thus revealing the formation of an H-bond. The density at the bond CP that characterizes the chalcogen bond is larger than that at the CP that characterizes the H-bond, thus suggesting that the chalcogen bond is energetically more favorable. We also performed the natural bond orbital analysis (NBO)[46] on this complex. We have focused our attention on the second order perturbation analysis since it is very convenient for the evaluation of donor–acceptor interactions from an orbital point of view.[47] We have found two donor–acceptor orbital interactions involving the N-atom of the dianionic ligand as the donor and the DMSO molecule as the acceptor. As typically in chalcogen bonds, there is an electron donation from the LP orbital of the N atom to the antibonding σ*(S–C) orbital with a concomitant stabilization energy of $E^{(2)} = 3.01$ kJ mol^{-1}. This energy is modest due to the small polarization of the S–C bond. For the H-bond, we have also found an electron donation from the LP orbital of the N atom to the antibonding σ*(C–H) orbital with a concomitant stabilization energy of $E^{(2)} = 0.33$ kJ mol^{-1}. This result agrees well with the electron charge density at the bond CP which is larger for the chalcogen bond.

In compound 2, we have analyzed the C–H⋯Ni(II) interactions that are established between the anionic and cationic fragments in the crystal structure, as indicated in Fig. 14a. The short Ni⋯H distance indicates that in addition to the electrostatic attraction between the counter-ions, the final geometry of the assembly could be modulated by this interaction. We wonder if it is an agostic interaction where the C–H sigma bond acts as an electron donor to the empty d orbital of Ni(II)
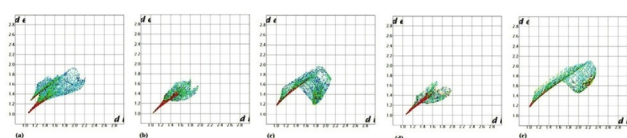

Fig. 12 View of the 2D finger print plots for the nickel center in (a) 1, (b) 2B, (c) 2A, (d) 3B, and (e) 3A.
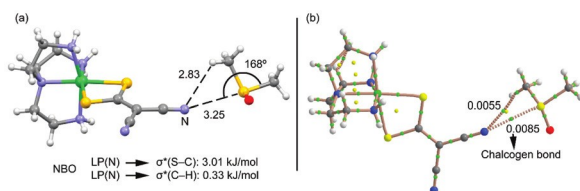

Fig. 13 (a) X-ray fragment with the indication of the combination of chalcogen and hydrogen bonds. Distances in Å. The results from the NBO calculations are also indicated. (b) Distribution of bond and ring CPs (green and yellow spheres, respectively) for the dimer. The values of ρ(r) at the bond CPs are given in a.u.

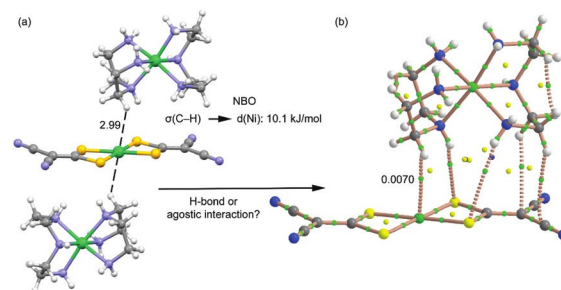Fig. 14 (a) X-ray fragment of compound 2 with the indication of the C–H⋯Ni(II) interaction. Distance in Å. The result from the NBO calculations is also indicated. (b) Distribution of bond, ring and cage CPs (green, yellow and blue spheres, respectively) for a dimer extracted from the assembly. The value of ρ(r) at the bond CP is given in a.u.

or if it is a hydrogen bonding interaction where the dianionic moiety acts as an electron donor using a filled d orbital of Ni(II) (the unconventional H-bond). The QTAIM distribution of the bond CPs and bond paths confirms the existence of the interaction (Fig. 14b) since a bond CP and bond path connect the Ni atom to the H-atom. The supramolecular complex is further characterized by four bond CPs and bond paths connecting several H-atoms of the cationic fragment to the i-mnt^{-2} ligand. The NBO analysis confirms the agostic nature of this interaction since only one orbital donor–acceptor interaction is found where the orbital of the σ(C–H) bond donates electrons to the empty d atomic orbital of Ni(II) with a concomitant stabilization energy of $E^{(2)} = 10.1$ kJ mol^{-1}, thus confirming the importance of the agostic interaction.

In compound 3, we have studied the intramolecular anion···π interaction that is established between the dianionic ligand and o-phenylenediamine (Fig. 15a). This interaction likely influences the shape of the polymeric chain. In principle the anion···π interaction is not favored in electron rich rings like o-phenylenediamine, however the coordination of the amino groups to the Ni(II) metal center increases the π-acidity of the ring. Since the solid state structure is polymeric, we have used a reduced theoretical model for the calculations (Fig. 15b). The QTAIM analysis shows that indeed the S atom interacts with the π-system of the aromatic ligand (the bond path connects the S atom to one C atom of the ring). The NBO analysis shows that the interaction is very weak (in terms of orbital contribution) since the electron donation from the LP of the S atom to the antibonding π-orbital of one C=C bond is only $E^{(2)} = 1.42$ kJ mol^{-1} in agreement with the small value of ρ(r) at the bond CP (0.0035 a.u.).

Electrochemical study

Cyclic voltammetry was used to understand the behaviour of compounds 1, 2 and 3 under reductive conditions. Solutions of all three compounds were prepared at a concentration of 0.1 mM in a 0.1 M acetonitrile solution of tetrabutylammonium hexafluorophosphate. A small sample of ferrocene (Fc) was added as an internal standard and scans were taken at potentials from −1.8 to +1 V using a glassy carbon working electrode, a platinum counter electrode, and a silver reference electrode. The resulting graphs were adjusted to the standard hydrogen electrode (SHE) by correcting the position of the Fc$^+$/Fc redox couple.[48] Compounds 1, 2 and 3 exhibit non-reversible reduction peaks at −1.62, −0.70 and −0.85 V vs. the SHE, respectively (Fig. 16). Given that compounds 2 and 3 both have square planar arrangements about the Ni center, it comes as no surprise that they are easier to reduce than octahedral compound 1. These two easier to reduce complexes are also shown to have greater catalytic ability for photocatalytic water reduction reactions.

Catalytic study

Compounds 1, 2, and 3 were tested for their catalytic activity in a high throughput photoreactor measuring hydrogen evolution from an iridium photosensitized water reduction reaction. The use of this system enabled rapid screening over concentration ranges for the PS and the nickel species. Initial testing in a concentration range from 0.1 to 1.5 mM for the WRCs revealed that the activity was greater at a lower concentration, so the range of 0.01 to 0.1 mM was chosen for further testing (Fig. 17). This range illustrates that these catalysts need a little concentration to generate a substantial amount of hydrogen and are most active in this low range.

While all three compounds were highly active catalysts, compounds 2, and 3, which have a square planar arrangement around the nickel center(s), were found to be the most active ones, attaining turnover numbers (TON) of 1000 and 1119,
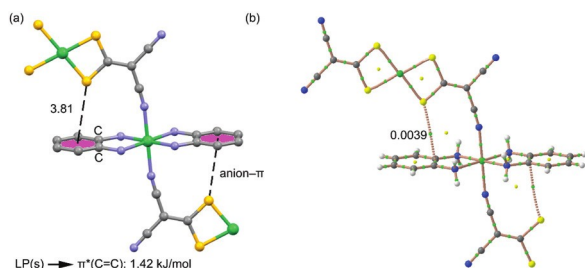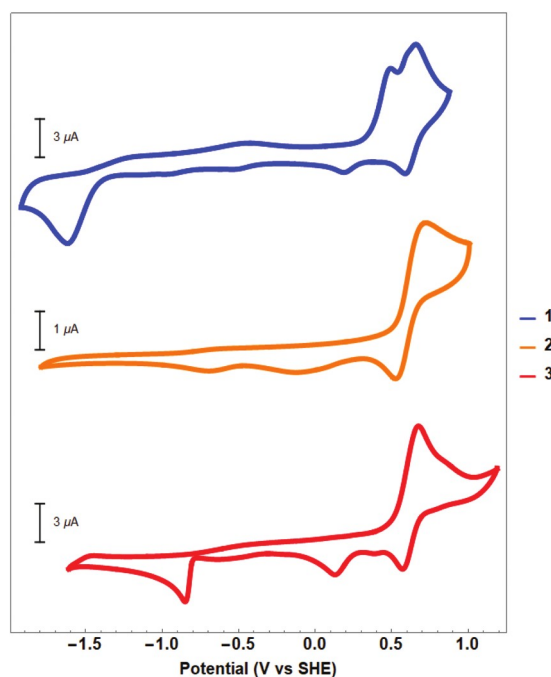

Fig. 15 (a) X-ray fragment of compound 3 with the indication of the anion–π interaction. Distance in Å to the ring centroid. The result from the NBO calculations is also indicated. (b) Distribution of bond and ring CPs (green and yellow spheres, respectively) for the dimer extracted from the assembly. The value of ρ(r) at the bond CP is given in a.u.

Fig. 16 Cyclic voltammograms for compounds 1, 2 and 3 recorded in acetonitrile with potentials corrected to the SHE through the positioning of the Fc$^+$/Fc couple. Scale bars for the current for each scan are placed next to each scan indicating the current in micro-amps.
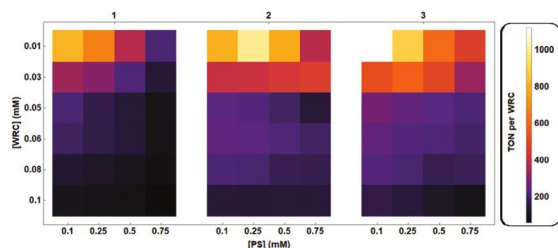
Fig. 17 Catalytic activity in photocatalytic water reduction reactions using compounds 1, 2, and 3 at varying concentrations with [Ir(Fmppy)$_2$dtbbpy PF$_6$] as the PS. Reactions examined through photometric detection and results reported as turnover numbers (TON) based on the content of the WRC.

respectively. Both the values were obtained at the lowest catalyst loading measured (0.01 mM), further indicating the potential of these systems to operate under ideal low loading conditions.

Conclusions

This work focuses on the synthesis, supramolecular structural elucidation by X-ray diffraction and optimization by QTAIM, NBO, and HS analyses of Ni(II) complexes prepared from dithiolate–polyamine based binary ligand systems and their catalytic activity in hydrogen evolution from the iridium photosensitized water reduction reaction. The single crystal X-ray diffraction analysis reveals the direct impact of binary ligand systems on the coordination pattern of the Ni(II) metal center imparting supramolecular arrangements involving the discrete formation of square planar and octahedral geometries in 1–3. In 1, tripodal flexible chelate tetraen coordinated to Ni^{+2} in a trichelated fashion and i-mnt^{-2} via thiolate ends revealing a slightly distorted octahedral geometry and one solvent molecule (DMSO) disordered over two positions forms N–H···O type hydrogen bonds imparting the crystal stability. The secondary ligand tren influences the coordination modes of i-mnt^{-2} to Ni^{+2} revealing square planar (NiS$_4$) and octahedral (NiN$_6$) geometries in the cocrystallised aggregates of 2, whereas in the presence of opda, i-mnt^{-2} behaves as an S,S,N-tridentate connector forming 1D polymeric chains bearing consecutive square planar (NiS$_4$) and octahedral (NiN$_6$) coordination kernels. The significance of DMF solvent molecules lies in the fact that they form 2D supramolecular chains via N3–H3A···O1 hydrogen bonds between the parallel polymeric chains along the bc plane imparting the substantial stability to the crystal packing arrangement. All the hydrogen bonds in 1–3 are well corroborated by the Hirshfeld surface analysis at the molecular level. Except 1, the N···H/H···N interactions around 2.2 Å < d_e + d_i < 2.8 Å predominate over the S···H/H···S interactions around 2.4 Å < d_e + d_i < 3.2 Å for all the coordination kernels that were examined separately by the HS analysis. The same trend is further confirmed by the HS analysis of the Ni^{+2} metal centers. The data from the 2D FP plots prove

that apart from H···H and other minor contacts, the hydrogen bond interactions account for more than 50% (1, 61.7%; 2A, 86%; 2B, 72%; 3A, 86.1%; 3B, 65.5%) of all the non-covalent contacts which act as a driving force in supramolecular crystal packing. The Ni···H contact (3.5%) opens up the possibility of C–H···Ni interaction (2.966 Å) between the square planar (2A) and octahedral (2B) kernels in 2 which is further confirmed by QTAIM optimization. QTAIM and NBO optimizations at the B3LYP/def2-TZVP level reveal the unorthodox interactions in the form of σ-hole chalcogen bonding interactions between the cyano end of i-mnt^{-2} and S-atom of the DMSO in 1, agostic interaction between the σ(C–H) bond and empty d-orbital of Ni(II) with a concomitant stabilization energy of E$^{(2)}$ = 10.1 kJ mol^{-1} in 2, and very weak anion···π interaction between the LP of the thiolate–S atom and the antibonding π-orbital of one C═C bond (the phenyl ring of opda) [E$^{(2)}$ = 1.42 kJ mol^{-1}] in 3. The applicability of 1–3 as highly active water reduction co-catalysts (WRCs) in the photo-catalytic hydrogen evolution process is well proved from the high turnover numbers (TONs) (2 and 3 are the most active ones with TONs of 1000 and 1119, respectively).

Conflicts of interest

There are no conflicts to declare.

Notes and references

1 (a) P. Jayaraman, S. F. Ni and D. Li, Coord. Chem. Rev., 2020, 420, 213398; (b) K. Tanifuji and Y. Ohki, Chem. Rev., 2020, 120, 5194; (c) M. Drosou, F. Kamatsos and C. A. Mitsopoulou, Inorg. Chem. Front., 2020, 7, 37; (d) R. R. Nasaruddin, T. Chen, N. Yan and J. Xie, Coord. Chem. Rev., 2018, 368, 60.
2 (a) C. A. Bolos, A. T. Chaviara, D. Mourelatos, Z. Iakovidou, E. Mioglou, E. Chrysogelou and A. Papageorgiou, Bioorg. Med. Chem., 2009, 17(35), 3142; (b) P. Deplano, L. Pilia,

D. Espa, M. L. Mercuri and A. Serpe, Coord. Chem. Rev., 2010, 254, 1434; (c) G. Li, M. F. Mark, H. Lv, D. W. McCamant and R. J. Eisenberg, J. Am. Chem. Soc., 2018, 140, 2575; (d) M. R. Carlson, D. L. Gray, C. P. Richers, W. Wang, P.-H. Zhao, T. B. Rauchfuss, V. Pelmenschikov, C. C. Pham, L. B. Gee, H. Wang and S. P. Cramer, Inorg. Chem., 2018, 57, 1988; (e) G. Cioncoloni, S. Sproules, C. Wilson and M. D. Symes, Eur. J. Inorg. Chem., 2017, 3707.

3 (a) T. Liu, W. Meng, Q.-Q. Ma, J. Zhang, H. Li, S. Li, Q. Zhao and X. Chen, Dalton Trans., 2017, 46, 4504; (b) Z. Chi, S. Takada, M. Kölzer, T. Matsumoto and K. Tatsumi, Angew. Chem., Int. Ed., 2006, 45, 3768; (c) N. Yuan, C. Tian, T. Sheng, S. Hu and X. Wu, Cryst. Growth Des., 2018, 18(5), 2667; (d) B. P. Biswal, H. A. Vignolo-González, T. Banerjee, L. Grunenberg, K. Gottschling, J. Nuss and B. V. Lotsch, J. Am. Chem. Soc., 2019, 141(28), 11082; (e) W. Zhang, J. Hong, J. Zheng, Z. Huang, J. Zhou and R. Xu, J. Am. Chem. Soc., 2011, 133, 20680.

4 (a) H. S. Shafaat, O. Rudiger, H. Ogata and W. Lubitz, Biochim. Biophys. Acta, 2013, 1827, 986; (b) B. L. Greene, C. H. Wu, G. E. Vansuch, M. W. Adams and R. B. Dyer, Biochemistry, 2016, 55, 1813.

5 (a) Z. Han, W. R. McNamara, M.-S. Eum, P. L. Holland and R. Eisenberg, Angew. Chem., Int. Ed., 2012, 51, 1667; (b) Z. Han, L. Shen, W. W. Brennessel, P. L. Holland and R. Eisenberg, J. Am. Chem. Soc., 2013, 135, 14659.

6 (a) M. K. Singh, S. Sutradhar, B. Paul, S. Adhikari, F. Laskar, R. J. Butcher, S. Acharya and A. Das, J. Mol. Struct., 2017, 1139, 395; (b) M. K. Singh, S. Sutradhar, B. Paul, S. Adhikari, F. Laskar, S. Acharya, D. Chakraborty, S. Biswas, A. Das, S. Roy and A. Frontera, J. Mol. Struct., 2018, 1139, 334; (c) S. Adhikari, T. Bhattacharjee, P. Nath, A. Das, J. P. Jasinski, R. J. Butcher and D. Maiti, Inorg. Chim. Acta, 2020, 119877; (d) S. Adhikari, T. Bhattacharjee, R. Gupta, C.-G. Daniliuc, M. Montazerozohori, R. Naghiha and A. Masoudiasl, Polyhedron, 2020, 192, 114838; (e) S. Adhikari, T. Bhattacharjee, A. Das, S. Roy, C.-G. Daniliuc, J. K. Zaręba, A. Bauzá and A. Frontera, CrystEngComm, 2020, 22, 8023; (f) T. Mochida, K. Takazawa, H. Matsui, M. Takahashi, M. Takeda, M. Sato, Y. Nishio, K. Kajita and H. Mori, Inorg. Chem., 2005, 44, 8628; (g) H. H. Alkam, A. Hatzidimitriou, C. C. Hadjikostas and C. Tsiamis, Inorg. Chim. Acta, 1997, 256, 41–50.

7 B. S. Kang, Z. N. Chen, C. Y. Su, Z. Lin and T. B. Wen, Polyhedron, 1998, 17, 2497.

8 (a) J.-M. Lehn, Supramolecular Chemistry: Concepts and Perspectives, VCH, Weinheim, 1995; (b) Molecular Self Assembly-Organic Versus Inorganic Approaches, Structure and Bonding, ed. M. Fujita, Springer, Berlin, 2000, vol. 96; (c) S. Adhikari, D. Kar, R. Fröhlich and K. Ghosh, ChemistrySelect, 2019, 4, 12825; (d) In.-W. Park, J. Yoo, S. Adhikari, J. S. Park, J. L. Sessler and C. H. Lee, Chem. – Eur. J., 2012, 18, 15073; (e) K. Ghosh, S. Adhikari, R. Frohlich, I. D. Petsalakis and G. Theodorakopoulos,

J. Mol. Struct., 2011, 1004, 193; (f) K. Ghosh, S. Adhikari and R. Frohlich, Tetrahedron Lett., 2008, 49, 5063; (g) K. Ghosh and S. Adhikari, Tetrahedron Lett., 2006, 47, 3577; (h) I.-W. Park, J. Yoo, S. Adhikari, S. K. Kim, Y. Yeon, C. J. E. Haynes, J. L. Sutton, C. C. Tong, V. M. Lynch, J. L. Sessler, P. A. Gale and C. H. Lee, Chem. – Eur. J., 2012, 18, 2514; (i) K. Ghosh, S. Adhikari, A. P. Chattopadhyay and P. R. Chowdhury, Beilstein J. Org. Chem., 2008, 4, 52.

9 (a) V. Mdluli, S. Diluzio, J. Lewis, J. F. Kowalewski, T. U. Connell, D. Yaron, T. Kowalewski and S. Bernhard, ACS Catal., 2020, 10, 6977; (b) I. N. Mills, J. A. Porras and S. Bernhard, Acc. Chem. Res., 2018, 51, 352; (c) J. H. Shon, S. Sittel and T. S. Teets, ACS Catal., 2019, 9, 8646; (d) J. H. Shon and T. S. Teets, Comments Inorg. Chem., 2020, 40, 53–85.

10 (a) S. Metz and S. Bernhard, Chem. Commun., 2010, 46, 7551; (b) P. N. Curtin, L. L. Tinker, C. M. Burgess, E. D. Cline and S. Bernhard, Inorg. Chem., 2009, 48, 10498; (c) A. Fihri, V. Artero, A. Pereira and M. Fontecave, Dalton Trans., 2008, 5567; (d) Y. Wang, X. Zhao, Y. Zhao, T. Yang, X. Liu, J. Xie, G. Li, D. Zhu, H. Tan and Z. Su, Dyes Pigm., 2019, 170, 107547.

11 (a) S. Diluzio, V. Mdluli, T. U. Connell, J. Lewis, V. VanBenschoten and S. Bernhard, J. Am. Chem. Soc., 2021, 143, 1179; (b) M. Yang, J. E. Yarnell, K. E. Roz and F. N. Castellano, ACS Appl. Energy Mater., 2020, 3, 1842; (c) K. Dedeian, J. Shi, N. Shepherd, E. Forsythe and D. C. Morton, Inorg. Chem., 2005, 44, 4445; (d) S. Lamansky, P. Djurovich, D. Murphy, F. Abdel-Razzaq, H. E. Lee, C. Adachi, P. E. Burrows, S. R. Forrest and M. E. Thompson, J. Am. Chem. Soc., 2001, 123, 4304; (e) F. Neve, M. La Deda, A. Crispini, A. Bellusci, F. Puntoriero and S. Campagna, Organometallics, 2004, 23, 5856.

12 (a) R. Henning, W. Schlamann and H. Kisch, Angew. Chem., Int. Ed. Engl., 1980, 19, 645; (b) E. Hontzopoulos, E. Vrachnou-Astra, J. Konstantatos and D. Katakis, J. Photochem., 1985, 30, 117; (c) A. Das, Z. Han, W. W. Brennessel, P. L. Holland and R. Eisenberg, ACS Catal., 2015, 5, 1397.

13 (a) J. Schneider, H. F. Jia, K. Kobiro, D. E. Cabelli, J. T. Muckerman and E. Fujita, Energy Environ. Sci., 2012, 5, 9502; (b) B. J. Fisher and R. Eisenberg, J. Am. Chem. Soc., 1980, 102, 361; (c) L. L. Efros, H. H. Thorp, G. W. Brudvig and R. H. Crabtree, Inorg. Chem., 1992, 31, 1722.

14 (a) W. Zhang, J. Hong, J. Zheng, Z. Huang, J. Zhou and R. Xu, J. Am. Chem. Soc., 2011, 133, 20680; (b) H. H. Cui, J. Y. Wang, M. Q. Hu, C. B. Ma, H. M. Wen, X. W. Song and C. N. Chen, Dalton Trans., 2013, 42, 8684; (c) H. N. Kagalwala, E. Gottlieb, G. Li, T. Li, R. Jin and S. Bernhard, Inorg. Chem., 2013, 52, 9094.

15 K. A. Jensen and L. Henriksen, Acta Chem. Scand., 1968, 22, 1107.

16 R. W. W. Hooft, Bruker AXS, 2008, Delft, The Netherlands.

17 Z. Otwinowski and W. Minor, Methods Enzymol., 1997, 276, 307.

18 Z. Otwinowski, D. Borek, W. Majewski and W. Minor, Acta Crystallogr., Sect. A: Found. Crystallogr., 2003, 59, 228.

19 G. M. Sheldrick, Acta Crystallogr., Sect. A: Found. Adv., 2015, 71, 3.

20 G. M. Sheldrick, Acta Crystallogr., Sect. C: Struct. Chem., 2015, 71(1), 3.

21 M. A. Spackman and P. G. Byrom, Chem. Phys. Lett., 1997, 267, 215.

22 J. J. McKinnon, M. A. Spackman and A. S. Mitchell, Acta Crystallogr., Sect. B: Struct. Sci., 2004, 60, 627.

23 J. J. McKinnon, D. Jayatilaka and M. A. Spackman, Chem. Commun., 2007, 3814.

24 M. A. Spackman and D. Jayatilaka, CrystEngComm, 2009, 11, 19.

25 M. J. Turner, J. J. McKinnon, S. K. Wolff, D. J. Grimwood, P. R. Spackman, D. Jayatilaka and M. A. Spackman, Crystal Explorer17, University of Western Australia, 2017.

26 T. A. Keith, AIMAll (Version 13. 05.06), TK Gristmill Software, Overland Park KS, USA, 2013.

27 M. J. Frisch, G. W. Trucks, H. B. Schlegel, G. E. Scuseria, M. A. Robb, J. R. Cheeseman, G. Scalmani, V. Barone, B. Mennucci, G. A. Petersson, H. Nakatsuji, M. Caricato, X. Li, H. P. Hratchian, A. F. Izmaylov, J. Bloino, G. Zheng, J. L. Sonnenberg, M. Hada, M. Ehara, K. Toyota, R. Fukuda, J. Hasegawa, M. Ishida, T. Nakajima, Y. Honda, O. Kitao, H. Nakai, T. Vreven, J. A. Montgomery Jr., J. E. Peralta, F. Ogliaro, M. Bearpark, J. J. Heyd, E. Brothers, K. N. Kudin, V. N. Staroverov, R. Kobayashi, J. Normand, K. Raghavachari, A. Rendell, J. C. Burant, S. S. Iyengar, J. Tomasi, M. Cossi, N. Rega, J. M. Millam, M. Klene, J. E. Knox, J. B. Cross, V. Bakken, C. Adamo, J. Jaramillo, R. Gomperts, R. E. Stratmann, O. Yazyev, A. J. Austin, R. Cammi, C. Pomelli, J. W. Ochterski, R. L. Martin, K. Morokuma, V. G. Zakrzewski, G. A. Voth, P. Salvador, J. J. Dannenberg, S. Dapprich, A. D. Daniels, Ö. Farkas, J. B. Foresman, J. V. Ortiz, J. Cioslowski and D. J. Fox, Gaussian 09 (Revision B.01), Gaussian, Inc., Wallingford CT, 2009.

28 (a) E. M. Lopato, E. A. Eikey, Z. C. Simon, S. Back, K. Tran, J. Lewis, J. F. Kowalewski, S. Yazdi, J. R. Kitchin, Z. W. Ulissi, J. E. Millstone and S. Bernhard, ACS Catal., 2020, 10, 4244; (b) W. Song, E. M. Lopato, S. Bernhard, P. A. Salvador and G. S. Rohrer, Appl. Catal., B, 2020, 269, 118750; (c) R. N. Motz, E. M. Lopato, T. U. Connell and S. Bernhard, Inorg. Chem., 2021, 60, 774.

29 P. N. Curtin, L. L. Tinker, C. M. Burgess, E. D. Cline and S. Bernhard, Inorg. Chem., 2009, 48, 10498.

30 A. Grohmann and F. Knoch, Inorg. Chem, 1996, 35, 7932.

31 R. M. Kirchner, C. Mealli, M. Bailey, N. Howe, L. P. Torre, L. J. Wilson, L. C. Andrews, N. J. Rose and E. C. Lingafelter, Coord. Chem. Rev., 1987, 77, 89.

32 L. J. Wilson and N. J. Rose, J. Am. Chem. Soc., 1968, 90, 6041.

33 J. E. K. Huheey, E. A. Keiter and R. L. Keiter, Inorganic Chemistry, Principles of Structure and Reactivity, Harper Collins, New York, 1993, p. 482.

34 S. Adhikari, T. Bhattacharjee, R. J. Butcher, M. Porchia, M. De Franco, C. Marzano, V. Gandin and F. Tisato, Inorg. Chim. Acta, 2019, 498, 119098.

35 A. Okuniewski, D. Rosiak, J. Chojnacki and B. Becker, Polyhedron, 2015, 90, 47.

36 S. Das, C. H. Hung and S. Goswami, Inorg. Chem., 2003, 42, 8592.

37 A. Bondi, J. Phys. Chem., 1964, 68, 441.

38 A. Castiñeiras, I. García-Santos, J. M. González-Pérez, A. Bauzá, J. K. Zaręba, J. Niclós-Gutiérrez, R. Torres, E. Vílchez and A. Frontera, Cryst. Growth Des., 2018, 18, 6786.

39 G. Mahmoudi, J. K. Zaręba, A. Bauzá, M. Kubicki, A. Bartyzel, A. D. Keramidas, L. Butusov, B. Mirosław and A. Frontera, CrystEngComm, 2018, 20, 1065.

40 R. Banik, S. Roy, A. M. Kirillov, A. Bauza, A. Frontera, A. Rodriguez-Dieguez, J. M. Salas, W. Maniukiewicz, S. K. Das and S. Das, CrystEngComm, 2016, 18, 5647.

41 G. Mahmoudi, J. K. Zaręba, A. V. Gurbanov, A. Bauzá, F. I. Zubkov, M. Kubicki, V. Stilinović, V. Kinzhybalo and A. Frontera, Eur. J. Inorg. Chem., 2017, 4763.

42 A. Y. Meyer, J. Comput. Chem., 1986, 7, 144.

43 J. Rudnick and G. Gaspari, J. Phys. A: Math. Gen., 1986, 19, 191.

44 Y. S. Tan, A. Otero-de-la-Roza, M. M. Jotani and E. R. T. Tiekink, Cryst. Growth Des., 2020, 20, 3272.

45 C. B. Pinto, L. H. R. Dos Santos and B. L. Rodrigues, Cryst. Growth Des., 2020, 20, 4827.

46 E. D. Glendening, C. R. Landis and F. Weinhold, Wiley Interdisc. Rev.: Comput. Mol. Sci., 2012, 2, 1.

47 F. Weinhold and C. R. Landis, Valency and bonding: a natural bond orbital donor-acceptor perspective, Cambridge University Press, Cambridge, UK, 2005.

48 V. V. Pavlishchuk and A. W. Addison, Conversion constants for redox potentials measured versus different electrodes in acetonitrile solutions at 25 °C, Inorg. Chim. Acta, 2000, 298, 97–102.